CHEMISTRY OF MATERIALS

pubs.acs.org/cm Article

Modification of the Interlayer Coupling and Chemical Reactivity of Multilayer Graphene through Wrinkle Engineering

Xinyu Huang,[⋈] Wen Zhao,[⋈] Chongyang Zhu,[⋈] Xianjue Chen, Xu Han, Jie Xing, Lihong Bao, Lei Meng, Norman N. Shi, Peng Gao, Lei Liu, Xingjiang Zhou, Feng Xu,* Feng Ding,* and Yuan Huang*

Cite This: *Chem. Mater.* 2021, 33, 2506–2515 Read Online

ACCESS | Metrics & More | Article Recommendations | Supporting Information

ABSTRACT: Wrinkles are special surface corrugations in two-dimensional materials, which can be used to tune their electronic, optical, and chemical properties. There have been many studies focusing on the wrinkle of monolayers and few layers, while studies on wrinkle-induced effects of multilayer materials are rarely reported. In this work, we present a highly efficient fast-cooling method to create wrinkle networks in layered materials, such as multilayer graphene (MLG), MoS_2, etc. Due to the highly ordered stacking mode, the wrinkles fabricated on exfoliated graphene show high anisotropy. The wrinkles prefer to generate along armchair or zigzag alignments, which are demonstrated by hydrogen plasma-etched hexagonal pits. Theoretical analysis further proved that the preferential alignments of wrinkles are driven by minimization of the strain energy of the wrinkles and the van der Waals interactions between adjacent graphene layers. Our classical molecular dynamics simulation clearly reproduces the formation of wrinkles in multilayer graphene and reveals the alignment-dependent formation processes. Raman spectra measurements show that the intensity ratio of $2D^-/2D^+$ on MLG wrinkles is higher than that of the flat area. High-resolution transmission electron microscopy (HRTEM) images show that the interlayer distance increases from 3.34 Å on a flat area to 3.83 Å on wrinkled multilayer graphene. Hydrogen plasma etching results reveal that the chemical reactivity of carbon atoms on wrinkles is significantly higher than that on flat areas, especially at the junction of wrinkles. All of the experimental results indicate that the interlayer coupling becomes weak and chemical reactivity increases on MLG wrinkles. This work proposes a new wrinkle engineering method for tuning the physical and chemical properties of MLG, which has important implications for unveiling novel phenomena of many other layered materials under strain, such as layered metal chalcogenides, black phosphorus, etc.

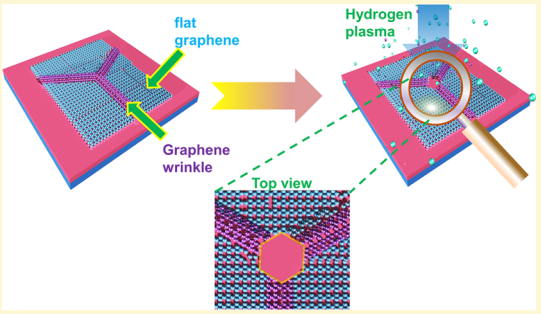

INTRODUCTION

In layered materials, many intrinsic properties depend strongly on interlayer coupling. Since interlayer coupling disappears in monolayers, the electronic structure of monolayers differs from that of multilayers and bulk crystals, especially for certain transition metal chalcogenide crystals, such as MoS_2, WS_2, WSe_2, etc., which show indirect to direct band gap transition from multilayers to monolayers.[1−3] Several methods have been developed for tuning the interlayer coupling in layered materials, such as controlling the number of layers,[4] making heterostructures,[5] and the newly developed twist angle strategy.[6−8] In the past decade, two-dimensional (2D) materials represented by graphene, hexagonal boron nitride (h-BN), and molybdenum disulfide (MoS_2) have been investigated intensively, and most breakthroughs were discovered on "flatland" materials, especially on monolayer and few-layer samples. As research progressed, interesting physical and chemical phenomena were discovered on nonplanar structures and multilayer crystals, which delivered new opportunities to develop fundamental understandings of these materials and to utilize them toward practical applications.[9−16] Wrinkles, as common nonplanar structures, can induce one-dimensional strain field and change the electrical and optical properties of 2D materials.[14,17] Besides, graphene wrinkles are special structures that help to understand the evolution between 2D graphene and one-dimensional (1D) carbon nanotubes. The interlayer coupling, chemical reactivity, and other electrical transport properties in 2D graphene and 1D carbon nanotubes have been well studied.[18−20] However, how wrinkles affect interlayer coupling and chemical reactivity is still waiting to be explored.

In this study, we report a fast-cooling method for making multilayer graphene (MLG) wrinkle network structures. The wrinkles exhibit a highly anisotropic morphology. Further characterization after hydrogen plasma etching treatment

Received: December 16, 2020
Revised: March 23, 2021
Published: April 5, 2021

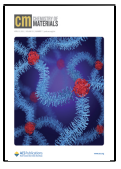

https://doi.org/10.1021/acs.chemmater.0c04799
Chem. Mater. 2021, 33, 2506−2515

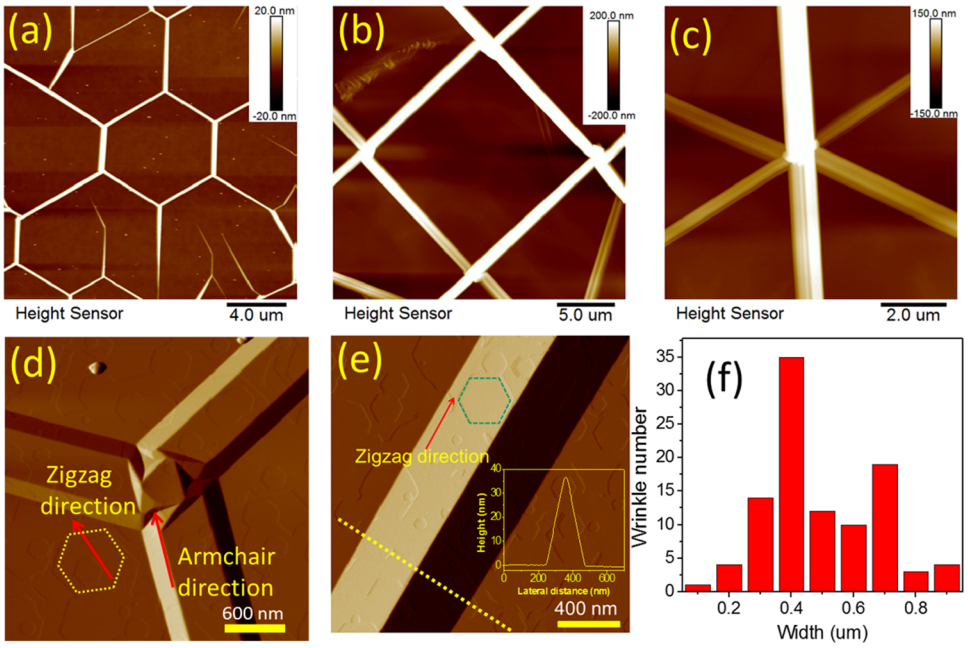

Figure 1. Morphology of graphene wrinkles in various geometric formations. AFM images of graphene wrinkles with different geometrical shapes, including hexagonal (a), square (b), and cross-linked (c). (d, e) AFM images of two different wrinkled graphene flakes measured in the amplitude error mode; the two flakes were etched by hydrogen plasma for 2 h. Hexagonal pits can be clearly seen in the two images, and the orientation of wrinkles can be determined by comparing them with the edge of hexagonal pits. (f) Distribution of wrinkles of varying wrinkle widths on graphene flakes with wrinkle networks.

shows that these wrinkles exhibit preferential symmetrical alignments along either zigzag or armchair orientation of the graphene lattice. Theoretical calculations verify that wrinkles along these two high symmetry alignments are energetically more favorable due to the low formation energies of the corresponding twins in MLG. The microscopic structure of multilayer graphene wrinkles was studied by transmission electron microscopy (TEM), from which the interlayer distance can be directly measured. TEM results clearly showed that the interlayer distance near the deformed area is larger than that of the flat area, which corresponds to a decrease in the interlayer coupling in the wrinkle region. Raman spectroscopy measurements on the wrinkles showed that the $2D^-$ peak increases, while the $2D^+$ peak decreases, which also points to the weakening of the interlayer coupling at the wrinkle region due to the increased distance between layers. After hydrogen plasma treatment, we discovered that the etching rate on wrinkles was higher than that on flat areas, which indicates that the highly deformed MLG is more chemically reactive than the flat area. A combination of experimental and calculation results presented in this study both confirmed and explained how wrinkle-induced strain field decreases interlayer coupling and increases chemical reactivity.

RESULTS AND DISCUSSION

Various corrugations in graphene/graphite can be created by loading different types of stress, for example, graphene bubble can be formed by applying biaxial tensile stress[10] and wrinkles can be generated by loading compressive stress. Poly(dimethylsiloxane) (PDMS) is a flexible organic material, which has been widely used for making buckled structures on graphene and metal films.[16,21] In the past decade, PDMS showed great potential in the field of flexible and wearable electronic device applications.[22,23] Here, we chose PDMS as the substrate for preparing multilayer graphene wrinkles.[24] As shown in Figure S1a, flat graphene flakes can be exfoliated onto solid substrates, such as SiO_2/Si and PDMS. By applying uniaxial stress from the substrate, some quasi-parallel wrinkles can be generated on multilayer graphene. Figure S1 shows the schematic and optical images of parallel graphene wrinkles. There have been a number of studies on graphene wrinkles fabricated by applying uniaxial stress; however, a biaxial stress-induced wrinkle structure has never been reported. Due to the large thermal expansion coefficient difference between graphene and PDMS,[25,26] biaxial compressive stress can be loaded on multilayer graphene flakes in liquid nitrogen. Figure S2a,b presents the schematic images for preparing wrinkle networks. Graphene flakes were relatively flat after exfoliating onto PDMS and only a few wrinkles could be observed. After dipping into liquid nitrogen, PDMS became so rigid and the MLG flakes "de-adhered" from the PDMS surface (Figure S3). Evidently, this de-adhesion ("de-pinning") happened after significant compressive stress drove wrinkle network formation in the MLG flakes. When PDMS was warmed back to room temperature, the flakes either did not "re-adhere" at all or they re-adhered once the PDMS became soft. Therefore, when PDMS was heated back up, there was no equivalent tensile stress during warming, as there was compressive stress during cooling. As can be seen in Figure S2c, graphene wrinkles intercept each other and show highly anisotropic morphology.

Atomic force microscopy (AFM) has been widely used to characterize the morphology and mechanical properties of nanomaterials, such as their thickness, surface roughness, and Young's modulus. Here, we used AFM to characterize the morphology of the wrinkle networks. As shown in Figure 1, different geometric configurations were observed on graphene wrinkle networks, such as hexagonal, square, cross-linked, and parallelogram structures (Figures 1a–c and S1). Although chemical vapor deposition (CVD)-grown graphene on metallic

https://doi.org/10.1021/acs.chemmater.0c04799
Chem. Mater. 2021, 33, 2506−2515

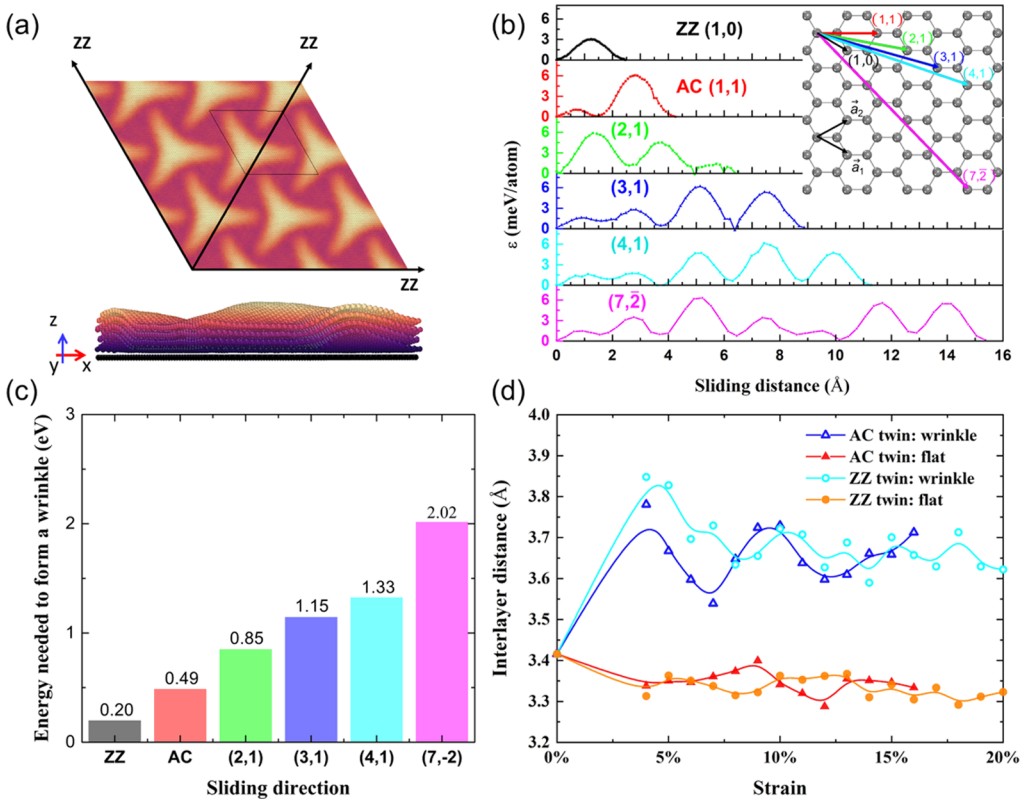

Figure 2. (a) Simulated model of wrinkles along the three ZZ alignments. (b) The energy profile for graphite sliding for a periodic length along different alignments. (c) The energy needed to form a wrinkle along different alignments. (d) The change in the interlayer distance in wrinkle and flat regions under increasing strain.

surfaces also shows widespread irregular wrinkles due to thermal expansion mismatch between graphene and the host,[27] highly regular (straight and along specific directions) graphene wrinkle network structures, as shown in Figure 1, have never been reported before. As can be seen in Figure 1, the alignments of wrinkles are not random, and they align preferentially along certain specific orientations. In Figure 1a, the angles between two intercepting wrinkles are close to 120° and a hexagonal pattern is clearly observed. The intercepting angles shown in Figure 1b are close to 90° and the wrinkles form a pattern of square lattices. In Figure 1c, three wrinkles intercept and all of the intercepting angles are 60°. Considering the six-fold symmetry of the graphene lattice, these observations suggest that the wrinkles in MLG tend to align along either the armchair or the zigzag direction of the graphene lattice. The height of these wrinkles ranges from tens of nanometers to hundreds of nanometers, depending on the thickness of the graphene flake (Figure 1f).

Hydrogen plasma is an effective way to etch graphene, which has been widely used for patterning special structures of graphene, like graphene nanoribbon, hexagonal pits, etc.[20,28] Here, we used hydrogen plasma to etch MLG flakes with induced wrinkles. Formation of hexagonal pits was observed on graphene flakes after etching, as can be clearly seen in Figure 1d,e. As shown in previous studies, the six edges of a hexagonal pit align along the zigzag (ZZ) orientation of the graphene lattice,[20] where the alignment of wrinkles in the graphite lattice can be assigned using the edges of the hexagonal pits as reference. As expected, we found that the wrinkles are along two dominating orientations, zigzag and armchair (Figure 1d,e). Figure 1d shows three wrinkles along the armchair direction. Wrinkles along the armchair orientation have been observed on graphene and h-BN flakes.[29,30] The wrinkle shown in Figure 1e is along the zigzag orientation. The lattice of graphite along the zigzag and armchair orientations has the smallest lattice constant, and therefore, a wrinkle along one of the two alignments will have the minimum formation energy and the smallest misalignment angle, which are 2.46 and 4.26 Å for the zigzag and armchair alignments, respectively.

Figure 2a shows a schematic model of wrinkles along three ZZ alignments by compressing four-layer graphene on the copper substrate with 3% biaxial strain. To better understand if the wrinkles form more easily along the ZZ and AC alignments, we calculated the energy profile of graphene sliding for a periodic length along different alignments using density functional theory (DFT) (Figure 2b), and the corresponding energy needed to form a wrinkle during sliding (Figures 2c and S4 and Table S1). The formation of wrinkles requires neighboring basal planes to slide past each other, which is driven by the energy minimization between the strain energy of the buckled region and the van der Waals (vdW) energy of adjacent layers. To minimize the latter, perfect commensurate layer stacking (ABA or ABC) away from the wrinkle is preserved. This leads to a periodic constraint on the magnitude of the slip ($|\Delta l|$) between each successive plane and also on the magnitude of the wrinkle angle, $\theta = \frac{|\Delta l|}{d} = \frac{i|\vec{a}|}{d}$, where d is the interlayer distance and $\vec{a}$ is the periodic length in the sliding direction.[29] As shown in the inset of Figure 2b, only sliding along the ZZ and AC alignments can have a small periodic length and minimize the energy loss (Figure 2b,c). This is why wrinkles are formed mostly along the ZZ and AC

https://doi.org/10.1021/acs.chemmater.0c04799
Chem. Mater. 2021, 33, 2506−2515

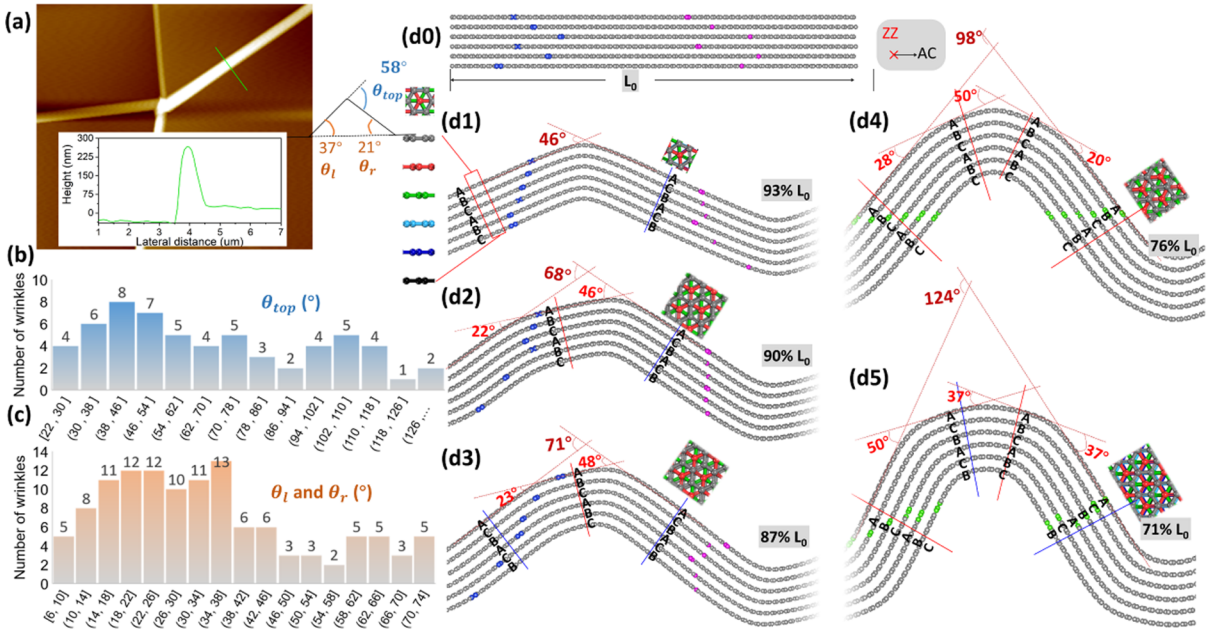

Figure 3. Mechanism of wrinkle formation. (a) AFM images of a typical graphene wrinkle. The left inset shows the height mapping across the wrinkle denoted by a black line. The right inset shows the angles of the wrinkle. (b) Statistics of the top angles of 60 wrinkles, θ_{top}. (c) Statistics of the bottom angles, θ_l and θ_r. (d0−d5) Snapshots of the molecular dynamics simulation of six-layer graphene compression from L_0 to 71% L_0. All colorful atoms are carbon. The blue and pink atoms are highlighted to denote the interlayer shift. Red and blue lines denote different stacking orders across the wrinkles. Insets show top and side views of the wrinkle, with different colors denoting carbon atoms in different layers.

directions. Figure 2d shows the change in the interlayer distance in the wrinkle and flat regions by increasing strain. The initial interlayer distance is 3.41 Å. As strain increases, the average interlayer distance increases and then fluctuates at around 3.65 Å in the buckled region, while it decreases to 3.32 Å in the flat region. The vdW interaction between layers is weakened in the wrinkle region, resulting in a decrease in the interlayer coupling. This observation is further confirmed by Raman spectroscopy, as discussed below.

To better understand the mechanism of wrinkle formation in MLG, we performed statistical analysis on the angles of 60 wrinkles and carried out molecular dynamic simulation. Figure 3a shows the AFM image of a typical wrinkle structure, and the height profile across the wrinkle. The top angle and the two bottom angles of the cross section are measured to be θ_{top} = 58°, θ_l = 37°, and θ_r = 21°, respectively, with the relationship $\theta_{top} = \theta_l + \theta_r$. The distribution of the top and bottom angles of all 60 wrinkles is summarized in Figure 3b,c, respectively. From these histograms, we observed that θ_{top} has a preferential distribution near 45°, and θ_l and θ_r are distributed around 25°. This is due to the favorable slip length $|\Delta l|$ and angles (θ_0 = 24, 46, and 65°) for wrinkles along the ZZ alignment between successive planes.[29] Figure 3d0−d5 shows six typical snapshots of molecular dynamics simulations of six-layer graphene compressed from L_0 to 71% L_0 along the AC orientation, with wrinkles forming along the ZZ orientation. Some atoms in the six layers are highlighted in blue, pink, and green to track the interlayer sliding. When the MLG is compressed to 93% L_0, a wrinkle forms along the ZZ direction with an angle θ of 46° (Figure 3d1). The flat regions next to the wrinkle are measured to be ABC stacking on the left and ACB stacking on the right. This is shown in the top view of the flat region in the insets of Figure 3d1; here, the stacking order of the second (red) and third layers (green) changes. As the model further compresses the MLG to 90% L_0, the total wrinkle angle θ increases to 68°, which consists of two smaller wrinkles, θ = 46 and 22°. The total angle θ will keep increasing to 71, 98, and finally 124° as the MLG is being compressed to 87, 76, and 71% L_0, respectively. In comparison, the individual wrinkle angles θ are relatively stable, mostly around ∼22, 37, and 48°. It is worth noting that as the MLG is being compressed, the number of individual wrinkles increases, and the flat regions between each wrinkle are always well stacked with alternate stacking orders. This simulation result confirms our model that the interlayer vdW interaction between flat regions and the strain energy in the wrinkle are competing and balancing factors. To lower the overall energy of the system under compression, the MLG generates these structured wrinkles along the ZZ and AC orientations to maintain the vdW interaction in the flat region.

The strain field has been widely used for tuning many intrinsic properties in layered materials, such as band gap in graphene[31,32] and photoluminescence behaviors in MX_2 systems (M = Mo, W, X = S, Se).[33−35] The physical and chemical behaviors around wrinkle areas are different from that of the flat areas, especially at the wrinkle junction zone. In Figure 1a−e, the junction parts show clear edges, indicating that the layered graphene is greatly distorted in this small area. The distorted junction with some areas lowered and some areas increased to keep the balance of the three wrinkles. From the microscopic point of view, the distorted strain will change the periodicity of carbon atoms' lattice, and the compression or expansion force can shorten or lengthen the C−C bonds at different sites, resulting in the change of the band structure of the layered material. As shown below, the chemical reactivity at the junction part is more active than that in the flat area.

Raman spectroscopy is a nondestructive characterization tool that has been extensively used to analyze layer numbers, interlayer coupling, and defects of graphene and other 2D materials.[36−38] The two dominant peaks in the graphene

https://doi.org/10.1021/acs.chemmater.0c04799
Chem. Mater. 2021, 33, 2506−2515

material, G and 2D, are sensitive to strain. In the presence of compressive or tensile strain, a relatively large ratio of $\Delta\omega_{2D}/\Delta\omega_G$ in the range of 2.02−2.44 is observed for graphene.[39,40] Uniaxial and biaxial strain can also be distinguished by Raman spectra.[41] Xu et al. found that the hexagonal atomic structure on the graphene wrinkle was distorted, which changed the vibration mode of the graphene crystal and also the electronic structure of graphene.[42] Here, we use Raman spectroscopy to detect the changes on wrinkled MLG (Figure 4). The Raman

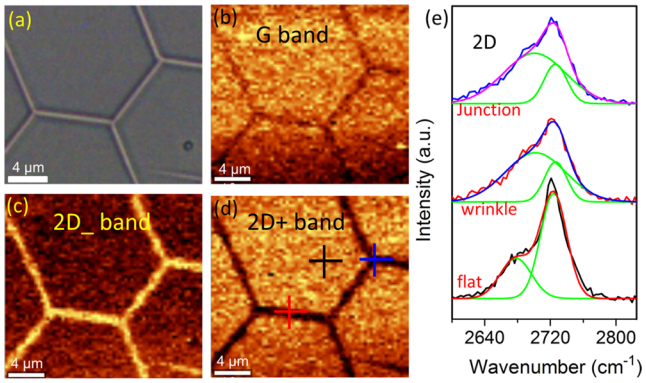

Figure 4. Raman measurement of graphene wrinkles. (a) Optical image of multilayer graphene wrinkles. (b) Raman mapping image of the G mode intensity for the wrinkles in (a). (c, d) Raman mapping images of $2D^-$ and $2D^+$ mode intensity; as can be clearly seen, the intensity of $2D^-$ on the wrinkle is higher than that on the flat area, while the intensity of the wrinkle is much lower than that of the flat area for the $2D^+$ mode. (e) Raman spectra of 2D modes measured at different sites, including the flat area, wrinkle, and wrinkle junction, which is shown in (d) by crosses. Two peaks were used to fit the 2D mode; both the relative intensity and half-width intensity are different for the flat area and the wrinkled area.

G band, located at 1580 cm^{-1}, is a dominant mode of graphene and graphite, which originates from the in-plane vibrational E_{2g} phonon. Figure 4b shows the G mode intensity mapping image of graphene wrinkles. The outline of the graphene wrinkle can still be seen in the G mode image when compared with the optical image in Figure 4a. The single spectrum of the G mode collected at different positions (flat area, wrinkle, and wrinkle junction as marked) is also presented in Figure S5. The position of the G mode in these three sites shows a negligible shift; however, the full width at half-maximum (FWHM) of the G peaks at different positions does vary, which are 15, 16, and 18 cm^{-1} for the flat area, wrinkle, and wrinkle junction, respectively. For single-layer graphene, the value of FWHM is roughly constant (12 cm^{-1}) as a function of strain,[41] whereas the FWHM of the G band in metallic nanotubes becomes much larger due to the increased electron−phonon coupling contribution.[43] Here, we need to emphasize that the Raman spectrum is an average signal that depends on the spot size of the laser (0.5 μm in diameter); however, from TEM results (Figure 5), we found that strain plays an important role only in a very confined area (few nanometers). This result indicates that the strain-induced Raman shift may not be observable by Raman spectroscopy if the strain is only localized in a small percentage of the total area covered by the laser spot. As a result, the peak position of the G band does not show an obvious shift, while the peak FWHM increases. Unlike the behavior of the G band, the 2D band is more sensitive to strain, which shows a clear difference for the wrinkle and the flat area from the 2D mode mapping image (Figure 4c−e). For simplicity, we divided the 2D peak into two peaks, $2D^-$ and $2D^+$, roughly 1/4 and 1/2 of the height of the G peak, respectively.[44] As shown in Figure 4e, the $2D^+$ mode is higher than the $2D^-$ mode in the flat area, and the half-widths for the two modes are 41.8 ($2D^-$) and 32.3 cm^{-1} ($2D^+$). However, the relative intensity ratio of $2D^-/2D^+$ increased from 30.2% on the flat area to 47.4% on the wrinkle and 57.2% on the wrinkle junction. The peak width of the $2D^-$ mode also showed an increase from 41.8 on the flat area to 57.8 and 61 cm^{-1} on the wrinkle and the wrinkle junction, respectively. Full spectrum details are summarized in Table 1. Due to the large size of the laser spot, we did not observe any obvious shift of both G and 2D modes on the wrinkle. It has been reported in studies that the G and 2D peaks of graphene move to higher wavenumbers under compressive strain,[45] while the two peaks shift to lower wavenumbers under tensile strain.[10,46] Here, in the wrinkled area, the deformation is localized to a single line less than 1 nm wide, shown in detail through TEM analysis in the following section. The signal that arises from strained graphene layers is a small fraction of the total Raman signal collected under the illuminated spot, which results in a broadened peak but negligible peak shift.

To get insights into the nanostructure of the graphene wrinkle, transmission electron microscopy (TEM) characterizations were performed. In Figure S6, top-view images show that graphene wrinkles exhibit a one-dimensional nature and are typically connected with each other. This result is in accordance with AFM observation that all graphene wrinkles eventually form into an integrated network. The high-resolution TEM (HRTEM) image and the corresponding Fourier transform (FFT) pattern show that the wrinkled region is slightly distorted, where the (002) plane (d = 0.34 nm) of the MLG crystal can be clearly distinguished, while the basal planes still maintain a perfect hexagonal crystal structure. Figure 5a further shows a typical TEM cross-sectional image of the MLG wrinkle, which exhibits a needle-like morphology, as indicated by the dashed yellow line. As shown in the magnified TEM image in Figure 5b, the top part of this wrinkle is similar to a multiwalled carbon nanotube. Graphene wrinkles with different shapes, such as triangular geometry, are also imaged in Figure S7. The difference in morphology is associated with the thickness of the graphene flake, as well as the strain imposed on graphene during wrinkle formation (Figure S8). Here, we take the needle-like wrinkle as an example to illustrate the structural changes under strain. From the enlarged TEM images (Figure S9a−c), a high degree of bending can be observed on graphene layers. This leads directly to the splitting of lattice fringes, as corroborated by FFT patterns with continuous diffraction rings (Figure 5b) or separate diffraction spots (Figure S9d−f). The diffraction ring of the (002) plane in FFT patterns shows some degree of ellipticity (the inset of Figure 5b), suggesting slight distortion of graphene layers on the wrinkle.

Further investigations on the evolution of lattice fringes conducted by HRTEM are shown in Figure 5d−h. The lattice spacing at the nonbending region is approximately 3.34 Å, which is in good agreement with the interlayer distance of the graphite crystal. However, the lattice spacing at the bending regions shows obvious variations, where the lattice spacing gradually increases from 3.47 to 3.83 Å along the direction of line 3 in Figure 5b. Similar observations were made at the bottom of the wrinkle (Figure S9g−k). Figure 5c summarizes

https://doi.org/10.1021/acs.chemmater.0c04799
Chem. Mater. 2021, 33, 2506−2515

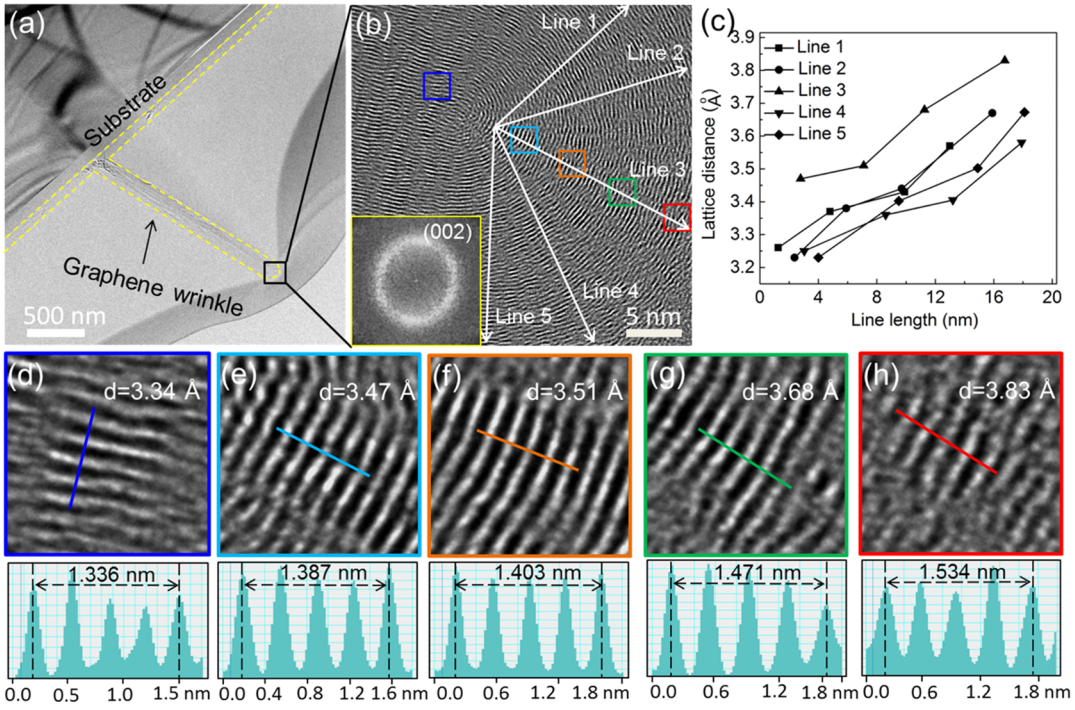

Figure 5. HRTEM characterization of graphene wrinkles. (a) Typical TEM cross-sectional image of the graphene wrinkle, which is nearly perpendicular to the graphene basal planes. (b) HRTEM image of the top region of the wrinkle, revealing that the lattice fringes split into an annular structure. The inset shows the corresponding FFT pattern with a continuous diffraction ring. (c) Statistical analysis of the change in lattice spacing along different alignments marked by white lines in (b). The vertical axis shows the difference in lattice spacing, while the horizontal axis represents the relative distance along each line. (d–h) HRTEM images of the selected areas marked by a colored box in (b), showing an increasing trend in lattice spacing along the alignment that the wrinkle bends outward.

Table 1. Peak Width, Intensity, and Intensity Ratio of $2D^-$ and $2D^+$ Peaks

position	peak width ($2D^-$, $2D^+$)	intensity ($2D^-$, $2D^+$)	intensity ratio of $2D^-/2D^+$ (%)
flat	41.8/32.3	33.4/110.6	30.2
wrinkle	57.8/36.5	41.0/86.5	47.4
wrinkle junction	61.0/38.6	50.3/87.9	57.2

the results from various directions to show the overall lattice spacing evolution, from which an increasing trend was confirmed along different directions, suggesting that the wrinkle bends outward (lines in Figure 5b). Extensive studies have established that the interlayer coupling in layered materials strongly depends on the interlayer distance. Compared with the flat area (Figure 5d), where the lattice spacing is 3.34 Å, the interlayer distance increased by 3.9, 5.1, 10.2, and 14.7% (Figure 5e–h, respectively). Such a huge interlayer distance change is quite striking in layered materials, which indicates that the interlayer coupling has decreased.

We also studied the chemical reactivity of wrinkled graphene by etching it in hydrogen plasma. Hydrogen plasma is a widely used anisotropic etching method for patterning graphene, where the plasma preferentially reacts with chemical active sites such as lattice defects, edges, and grain boundaries.[20,28] Changing the reactivity of the wrinkle offers a new perspective to selectively pattern graphene structures. As shown above, wrinkled graphene can be divided into three different areas: flat area, wrinkle, and wrinkle junction. It has been shown in this study that the atomic structure of the wrinkles with a large curvature is different from that of the flat area, and as a result, we expect some modification to its chemical reactivity as well. From the optical image of the plasma-treated sample shown in Figure 6a, we can infer that etched hexagonal pits start forming preferentially at the junction of wrinkles.

The Raman spectrum as well as the optical image (the inset of Figure 6b) indicate that the wrinkle junction was completely etched and formed a hexagonal pit after 10 h plasma treatment. The wrinkled parts are also etched but the Raman signal shows that graphene is still present. As presented in Figure 6b, the flat area shows a strong Raman signal (blue curve), indicating that this area was not etched as severely as the wrinkle junction and wrinkled areas. The Raman spectrum measured on the flat area is similar to that of graphite but shows a detectable D peak. The D peak at 1350 cm^{-1} can be detected both on the wrinkle and the flat area. The Raman intensity measured on the wrinkle is clearly weaker than the one measured on the flat area. This result indicates that the graphite atom structure has been broken severely on the wrinkle. Since the laser spot size of the laser (~1 μm) is larger than the width of the wrinkle (~100 nm), the signal of the G and 2D peaks on the flat area is partially collected. This result indicates that carbon atoms are more active in areas with larger strain, especially at the junction of the wrinkle, where the carbon atoms are being etched away at a much faster rate than on the flat area.

To better understand the increase in chemical reactivity in the wrinkle area, we performed DFT calculations to calculate the absorption energy of a hydrogen atom on the surface of few-layer graphene using the equation $E_b = E_{gra} + E_H - E_{H+gra}$. Higher E_b indicates the stronger absorption and higher chemical activity of graphene. As shown in Figure 6c,d, the absorption energies of H outside the wrinkle, inside the wrinkle, and on the flat region are 1.43, 0.78, and 1.26 eV,

https://doi.org/10.1021/acs.chemmater.0c04799
Chem. Mater. 2021, 33, 2506–2515

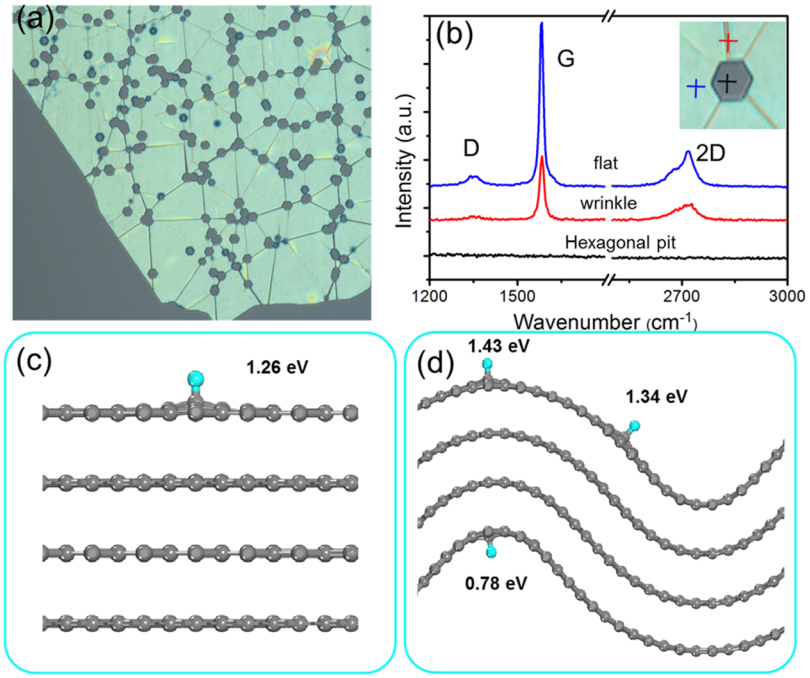

Figure 6. Selective etching of wrinkled graphene by hydrogen plasma. (a) Optical image of one wrinkled graphene flake after 10 h hydrogen plasma treatment. Hexagonal pits can be clearly seen at the junction of wrinkles, which indicates that the junction areas are more active than flat areas. (b) Raman spectra of wrinkled graphene after hydrogen plasma etching; the three curves were measured at the hexagonal pit (black), wrinkle (red), and flat area (blue), which were cross-marked in the inset image. (c, d) Hydrogen atoms (cyan) absorbed on the flat and curved surfaces of few-layer graphene (gray).

respectively. The higher chemical activity outside the wrinkle comes from the fact that its bond angle after H absorption closely resembles that of the sp^3 hybridization structure,[47] and the bonds outside are slightly stretched compared to those inside. Therefore, by engineering wrinkle structure on graphene, we can tune the chemical reactivity of multilayer graphene. We believe that the wrinkle-induced chemical enhancement is a universal phenomenon, which can also be applied for tuning the chemical reactivity of other layered materials, such as MoS_2, GaS, WSe_2, WS_2, etc. (Figure S10).

CONCLUSIONS

In summary, we developed a new fast-cooling method to generate wrinkle networks in multilayer graphene. By combining hydrogen plasma etching and AFM characterization, the preferential alignment of wrinkles in multilayer graphene is identified as armchair and zigzag, which is further confirmed through theoretical analysis and DFT calculations. These calculations showed that the preferential alignments of wrinkles are driven by minimization of the strain energy of the wrinkle and the vdW interactions between adjacent graphene layers. Our classical molecular dynamics simulation based on a newly developed potential energy surface clearly reproduced the formation of wrinkles in multilayer graphene and revealed the alignment-dependent formation processes. Comparing with the Raman signal on the flat area, there is no obvious G or 2D peak position shift in the wrinkle area, but the peak widths for both are greatly broadened, implying that there is no significant strain near the wrinkle area, but the AB stacking order in multilayer graphene is lost. More importantly, both Raman and TEM results demonstrate that the interlayer coupling on the wrinkle is weaker than that on the flat area. We discovered, for the first time, that the interlayer distance increases on the wrinkle, resulting in the decrease of interlayer coupling and changing of the band structure. Hydrogen plasma etching and DFT calculations showed that the chemical reactivity of graphene can be enhanced due to the increased curvature through wrinkle engineering. This fast-cooling method can be widely used to produce wrinkles in a variety of multilayer 2D materials and tune their chemical reactivity, which will serve as a springboard to achieve broader and deeper learning and understanding of multilayer 2D materials.

METHODS

Calculations. Density functional theory (DFT) calculations were performed with the Vienna Ab Initio Simulation Package (VASP).[48] The exchange-correlation functional was described by the Perdew–Burke–Ernzerhof version of generalized gradient approximation[49] and the core region by the projector augmented wave method[50] with the cutoff of the plane wave set as 400 eV. The Tkatchenko–Scheffler method[51] was used for the description of van der Waals (vdW) interaction. An $11 \times 11 \times 1$ k-point mesh was used for sliding bilayer graphene, and a $1 \times 1 \times 1$ k-point mesh was used for the absorption of hydrogen atoms on the wrinkle. The vacuum layer was larger than 8 Å to avoid interactions of neighboring images. Using the plane-wave-based total energy minimization, all structures were fully relaxed until the force on each atom was less than 0.001 eV/Å.

The carbon–carbon interaction was described by the second-generation reactive empirical bond order (REBO) potential[52] and the van der Waals interaction by a modified Lenard–Jones potential. During the molecular dynamics (MD) simulation, Newton's equation of atom's motion was integrated by the Velocity Verlet algorithm with a Berendsen thermostat[53] maintaining the temperature of the system at 300 K. The atomic model used a 32×14 supercell with six-layer AB stacking graphite. The supercell volume was $129.51 \times 34.55 \times 100$ $Å^3$. The periodical boundary condition was applied and the total number of atoms was 10 752. The time step was 1 fs and each compressing stage was annealed for 50 000 steps. The uniaxial strain was applied to compress the model to 95% of its original length first

https://doi.org/10.1021/acs.chemmater.0c04799
Chem. Mater. 2021, 33, 2506–2515

and then gradually compressed it by 1% every 50 ps during the simulation. To better analyze the stacking consequences, each MD simulation was followed by structure relaxation. The atomic model in Figure 3 is the structure after relaxation.

Sample Preparation and AFM Characterization. PDMS films were used as substrates to cleave relatively thick multilayer graphene (MLG) flakes through a process similar to the mechanical exfoliation of graphene.[54] Each of the PDMS/MLG flake samples was immersed in liquid nitrogen contained in a small Dewar for a given time. The sample was taken out of the Dewar after bubbling from PDMS had stopped (usually 5 s). After dipping into liquid nitrogen, PDMS became so rigid and MLG flakes de-adhered from the PDMS surface (Figure S3). Evidently, this de-adhesion (de-pinning) happened after significant compressive stress drove wrinkle network formation in the MLG flakes. When PDMS was warmed back to room temperature, the flakes either did not re-adhere at all or they re-adhered once the PDMS became soft. Therefore, when PDMS was heated back up, there was no equivalent tensile stress during warming, as there was compressive stress during cooling. For the graphene flakes prepared on the same PDMS, thinner flakes show higher wrinkle density, as shown in Figure S8. Optical microscopy (6XB-PC, Shang Guang) was used to capture the images of wrinkles. Wrinkles on the exfoliated flakes of other layered materials were prepared by the same method. AFM characterization of wrinkles was done with Bruker Dimension Edge and Asylum Research Cypher (AR Cypher) atomic force microscopes (AFM) in tapping and contacting modes, respectively.

Hydrogen Plasma Etching Experiments. Hydrogen plasma etching was carried out in a custom-made remote plasma system. Inductively coupled plasma was generated at one end of a 6.5 cm diameter quartz tube furnace using a radio frequency (RF) coil. The MLG flake samples with wrinkles transferred on a Si wafer with 300 nm thick thermal oxide layer were heated by placing them at the center of a furnace (400 °C), which was separated from the RF coil by a distance of about 20 cm. The plasma was generated outside the furnace and carried downstream to reach the sample. The pressure in the tube furnace was fixed at about 0.1 Torr with hydrogen flowing at 30 sccm under vacuum pumping.

Raman Measurements. Confocal Raman spectroscopy/microscopy (WITec α 300) was used to measure the spectra and geometry of the wrinkles formed in the MLG flakes. A laser wavelength of 532 nm and a spot size of ~0.5 μm were used to obtain the Raman spectra and mapping images.

TEM Measurements. The wrinkle sample for TEM measurements was prepared by focused ion beam microscopy (FIB, FEI DB235). The structure of the multilayer graphene wrinkle was studied by high-resolution transmission electron microscopy (HRTEM, FEI Titan3 G2 60-300).

■ ASSOCIATED CONTENT

Supporting Information

The Supporting Information is available free of charge at https://pubs.acs.org/doi/10.1021/acs.chemmater.0c04799.

Optical images of graphene wrinkles; wrinkle formation mechanism; G band Raman spectra of MLG in Figure 3a; top-view and cross-sectional TEM images of wrinkles; optical images of wrinkles of different layered materials fabricated by the fast-cooling method; and average energy for one C atom to slide a periodic length (PDF)

■ AUTHOR INFORMATION

Corresponding Authors

Feng Xu − *SEU-FEI Nano-Pico Center, Key Laboratory of MEMS of the Ministry of Education, Southeast University, Nanjing 210096, China;* orcid.org/0000-0001-7738-9673; Email: fxu@seu.edu.cn

Feng Ding − *Center for Multidimensional Carbon Materials (CMCM), Institute for Basic Science (IBS), Ulsan 44919, Republic of Korea*; Email: f.ding@unist.ac.kr

Yuan Huang − *Institute of Physics, Chinese Academy of Sciences, Beijing 100190, China; Advanced Research Institute of Multidisciplinary Science, Beijing Institute of Technology, Beijing 100081, China; Songshan Lake Materials Laboratory, Dongguan 523808, China;* orcid.org/0000-0002-7005-1319; Email: yhuang01@iphy.ac.cn

Authors

Xinyu Huang − *Institute of Physics, Chinese Academy of Sciences, Beijing 100190, China; Department of Materials Science and Engineering, College of Engineering, Peking University, Beijing 100871, China*

Wen Zhao − *Center for Multidimensional Carbon Materials (CMCM), Institute for Basic Science (IBS), Ulsan 44919, Republic of Korea;* orcid.org/0000-0002-1118-8155

Chongyang Zhu − *Center for Multidimensional Carbon Materials (CMCM), Institute for Basic Science (IBS), Ulsan 44919, Republic of Korea; SEU-FEI Nano-Pico Center, Key Laboratory of MEMS of the Ministry of Education, Southeast University, Nanjing 210096, China*

Xianjue Chen − *Center for Multidimensional Carbon Materials (CMCM), Institute for Basic Science (IBS), Ulsan 44919, Republic of Korea*

Xu Han − *Institute of Physics, Chinese Academy of Sciences, Beijing 100190, China; School of Science, China University of Geosciences, Beijing 100083, China*

Jie Xing − *School of Science, China University of Geosciences, Beijing 100083, China;* orcid.org/0000-0001-5350-6206

Lihong Bao − *Institute of Physics, Chinese Academy of Sciences, Beijing 100190, China;* orcid.org/0000-0002-2942-892X

Lei Meng − *Institute of Physics, Chinese Academy of Sciences, Beijing 100190, China; College of Science, Minzu University of China, Beijing 100081, China*

Norman N. Shi − *Department of Applied Physics and Applied Mathematics, Columbia University, New York 10027, United States*

Peng Gao − *Electron Microscopy Laboratory, School of Physics, Center for Nanochemistry, Peking University, Beijing 100871, China;* orcid.org/0000-0003-0860-5525

Lei Liu − *Department of Materials Science and Engineering, College of Engineering, Peking University, Beijing 100871, China*

Xingjiang Zhou − *Institute of Physics, Chinese Academy of Sciences, Beijing 100190, China*

Complete contact information is available at: https://pubs.acs.org/10.1021/acs.chemmater.0c04799

Author Contributions

⋈X. Huang, W.Z., and C.Z. contributed equally to this work.

Notes

The authors declare no competing financial interest.

■ ACKNOWLEDGMENTS

This work was supported by the National Key Research and Development Program of China (Grant Nos. 2019YFA0308000, 2018YFA0704201, and 2016YFA0300300), the National Natural Science Foundation of China (Grant Nos. 11874405, 62022089, 11504439,

51972058, and 11774051), the Youth Innovation Promotion Association of CAS (2019007), the Strategic Priority Research Program (B) of the Chinese Academy of Sciences (Grant No. XDB33000000), and the National Postdoctoral Program for Innovative Talents (BX20190067). The authors thank Prof. Ping Heng Tan, Dr. Kuan Zhang, and Dr. Miao Ling Lin for discussion and valuable comments.

REFERENCES

(1) Mak, K. F.; Lee, C.; Hone, J.; Shan, J.; Heinz, T. F. Atomically Thin MoS_2: A New Direct-Gap Semiconductor. *Phys. Rev. Lett.* **2010**, *105*, No. 136805.
(2) Zhao, W. J.; Ribeiro, R. M.; Toh, M. L.; Carvalho, A.; Kloc, C.; Neto, A. H. C.; Eda, G. Origin of Indirect Optical Transitions in Few-Layer MoS_2, WS_2, and WSe_2. *Nano Lett.* **2013**, *13*, 5627−5634.
(3) Zhao, W. J.; Ghorannevis, Z.; Chu, L. Q.; Toh, M. L.; Kloc, C.; Tan, P. H.; Eda, G. Evolution of Electronic Structure in Atomically Thin Sheets of WS_2 and WSe_2. *ACS Nano* **2013**, *7*, 791−797.
(4) Lee, Y.; Lee, J.; Bark, H.; Oh, I. K.; Ryu, G. H.; Lee, Z.; Kim, H.; Cho, J. H.; Ahn, J. H.; Lee, C. Synthesis of wafer-scale uniform molybdenum disulfide films with control over the layer number using a gas phase sulfur precursor. *Nanoscale* **2014**, *6*, 2821−2826.
(5) Zhang, J.; Wang, J. H.; Chen, P.; Sun, Y.; Wu, S.; Jia, Z. Y.; Lu, X. B.; Yu, H.; Chen, W.; Zhu, J. Q.; Xie, G. B.; Yang, R.; Shi, D. X.; Xu, X. L.; Xiang, J. Y.; Liu, K. H.; Zhang, G. Y. Observation of Strong Interlayer Coupling in MoS_2/WS_2 Heterostructures. *Adv. Mater.* **2016**, *28*, 1950−1956.
(6) Bistritzer, R.; MacDonald, A. H. Moire bands in twisted double-layer graphene. *Proc. Natl. Acad. Sci. U.S.A.* **2011**, *108*, 12233−12237.
(7) Cao, Y.; Fatemi, V.; Fang, S.; Watanabe, K.; Taniguchi, T.; Kaxiras, E.; Jarillo-Herrero, P. Unconventional superconductivity in magic-angle graphene superlattices. *Nature* **2018**, *556*, 43−50.
(8) Kim, K.; DaSilva, A.; Huang, S.; Fallahazad, B.; Larentis, S.; Taniguchi, T.; Watanabe, K.; Leroy, B. J.; MacDonald, A. H.; Tutuc, E. Tunable moire bands and strong correlations in small-twist-angle bilayer graphene. *Proc. Natl. Acad. Sci. U.S.A.* **2017**, *114*, 3364−3369.
(9) Levy, N.; Burke, S. A.; Meaker, K. L.; Panlasigui, M.; Zettl, A.; Guinea, F.; Neto, A. H. C.; Crommie, M. F. Strain-Induced Pseudo-Magnetic Fields Greater Than 300 Tesla in Graphene Nanobubbles. *Science* **2010**, *329*, 544−547.
(10) Huang, Y.; Wang, X.; Zhang, X.; Chen, X. J.; Li, B. W.; Wang, B.; Huang, M.; Zhu, C. Y.; Zhang, X. W.; Bacsa, W. S.; Ding, F.; Ruoff, R. S. Raman Spectral Band Oscillations in Large Graphene Bubbles. *Phys. Rev. Lett.* **2018**, *120*, No. 186104.
(11) Deng, S. K.; Berry, V. Wrinkled, rippled and crumpled graphene: an overview of formation mechanism, electronic properties, and applications. *Mater. Today* **2016**, *19*, 197−212.
(12) Bao, W. Z.; Miao, F.; Chen, Z.; Zhang, H.; Jang, W. Y.; Dames, C.; Lau, C. N. Controlled ripple texturing of suspended graphene and ultrathin graphite membranes. *Nat. Nanotechnol.* **2009**, *4*, 562−566.
(13) Cranford, S. W.; Buehler, M. J. Packing efficiency and accessible surface area of crumpled graphene. *Phys. Rev. B* **2011**, *84*, No. 205451.
(14) Zhu, W. J.; Low, T.; Perebeinos, V.; Bol, A. A.; Zhu, Y.; Yan, H. G.; Tersoff, J.; Avouris, P. Structure and Electronic Transport in Graphene Wrinkles. *Nano Lett.* **2012**, *12*, 3431−3436.
(15) Wu, Y.; Zhai, D.; Pan, C.; Cheng, B.; Taniguchi, T.; Watanabe, K.; Sandler, N.; Bockrath, M. Quantum Wires and Waveguides Formed in Graphene by Strain. *Nano Lett.* **2018**, *18*, 64−69.
(16) Wang, Y.; Yang, R.; Shi, Z. W.; Zhang, L. C.; Shi, D. X.; Wang, E.; Zhang, G. Y. Super-Elastic Graphene Ripples for Flexible Strain Sensors. *ACS Nano* **2011**, *5*, 3645−3650.
(17) Liu, Y. P.; Kenry; Guo, Y. F.; Sonam, S.; Hong, S. K.; Nai, M. H.; Nai, C. T.; Gao, L. B.; Chen, J. Y.; Cho, B. J.; Lim, C. T.; Guo, W. L.; Loh, K. P. Large-Area, Periodic, Hexagonal Wrinkles on Nanocrystalline Graphitic Film. *Adv. Funct. Mater.* **2015**, *25*, 5492−5503.
(18) Sui, Y.; Appenzeller, J. Screening and Interlayer Coupling in Multilayer Graphene Field-Effect Transistors. *Nano Lett.* **2009**, *9*, 2973−2977.
(19) Ohta, T.; Robinson, J. T.; Feibelman, P. J.; Bostwick, A.; Rotenberg, E.; Beechem, T. E. Evidence for Interlayer Coupling and Moire Periodic Potentials in Twisted Bilayer Graphene. *Phys. Rev. Lett.* **2012**, *109*, No. 186807.
(20) Yang, R.; Zhang, L. C.; Wang, Y.; Shi, Z. W.; Shi, D. X.; Gao, H. J.; Wang, E. G.; Zhang, G. Y. An Anisotropic Etching Effect in the Graphene Basal Plane. *Adv. Mater.* **2010**, *22*, 4014−4019.
(21) Bowden, N.; Brittain, S.; Evans, A. G.; Hutchinson, J. W.; Whitesides, G. M. Spontaneous formation of ordered structures in thin films of metals supported on an elastomeric polymer. *Nature* **1998**, *393*, 146−149.
(22) Li, Y. Q.; Zhu, W. B.; Yu, X. G.; Huang, P.; Fu, S. Y.; Hu, N.; Liao, K. Multifunctional Wearable Device Based on Flexible and Conductive Carbon Sponge/Polydimethylsiloxane Composite. *ACS Appl. Mater. Interfaces* **2016**, *8*, 33189−33196.
(23) Wang, X. W.; Gu, Y.; Xiong, Z. P.; Cui, Z.; Zhang, T. Silk-Molded Flexible, Ultrasensitive, and Highly Stable Electronic Skin for Monitoring Human Physiological Signals. *Adv. Mater.* **2014**, *26*, 1336−1342.
(24) Meng, L. Y.; Li, Y.; Liu, T. S.; Zhu, Z. Y.; Li, Q. Y.; Chen, X. J.; Zhang, S.; Zhang, X.; Bao, L. H.; Huang, Y.; Xu, F.; Ruoff, R. S. Wrinkle networks in exfoliated multilayer graphene and other layered materials. *Carbon* **2020**, *156*, 24−30.
(25) Yoon, D.; Son, Y. W.; Cheong, H. Negative Thermal Expansion Coefficient of Graphene Measured by Raman Spectroscopy. *Nano Lett.* **2011**, *11*, 3227−3231.
(26) Müller, A.; Wapler, M. C.; Wallrabe, U. A quick and accurate method to determine the Poisson's ratio and the coefficient of thermal expansion of PDMS. *Soft Matter* **2019**, *15*, 779−784.
(27) Sutter, P.; Sadowski, J. T.; Sutter, E. Graphene on Pt(111): Growth and substrate interaction. *Phys. Rev. B* **2009**, *80*, No. 245411.
(28) Shi, Z. W.; Yang, R.; Zhang, L. C.; Wang, Y.; Liu, D. H.; Shi, D. X.; Wang, E. G.; Zhang, G. Y. Patterning Graphene with Zigzag Edges by Self-Aligned Anisotropic Etching. *Adv. Mater.* **2011**, *23*, 3061−3065.
(29) Rooney, A. P.; Li, Z.; Zhao, W.; Gholinia, A.; Kozikov, A.; Auton, G.; Ding, F.; Gorbachev, R. V.; Young, R. J.; Haigh, S. J. Anomalous twin boundaries in two dimensional materials. *Nat. Commun.* **2018**, *9*, No. 3597.
(30) Oliveira, C. K.; Gomes, E. F. A.; Prado, M. C.; Alencar, T. V.; Nascimento, R.; Malard, L. M.; Batista, R. J. C.; de Oliveira, A. B.; Chacham, H.; de Paula, A. M.; Neves, B. R. A. Crystal-oriented wrinkles with origami-type junctions in few-layer hexagonal boron nitride. *Nano Res.* **2015**, *8*, 1680−1688.
(31) Ni, Z. H.; Yu, T.; Lu, Y. H.; Wang, Y. Y.; Feng, Y. P.; Shen, Z. X. Uniaxial Strain on Graphene: Raman Spectroscopy Study and Band-Gap Opening. *ACS Nano* **2008**, *2*, 2301−2305.
(32) Guinea, F.; Katsnelson, M. I.; Geim, A. K. Energy gaps and a zero-field quantum Hall effect in graphene by strain engineering. *Nat. Phys.* **2010**, *6*, 30−33.
(33) Castellanos-Gomez, A.; Roldan, R.; Cappelluti, E.; Buscema, M.; Guinea, F.; van der Zant, H. S. J.; Steele, G. A. Local Strain Engineering in Atomically Thin MoS_2. *Nano Lett.* **2013**, *13*, 5361−5366.
(34) Luo, S. W.; Hao, G. L.; Fan, Y. P.; Kou, L. Z.; He, C. Y.; Qi, X.; Tang, C.; Li, J.; Huang, K.; Zhong, J. X. Formation of ripples in atomically thin MoS_2 and local strain engineering of electrostatic properties. *Nanotechnology* **2015**, *26*, No. 105705.
(35) Wang, Y. L.; Cong, C. X.; Yang, W. H.; Shang, J. Z.; Peimyoo, N.; Chen, Y.; Kang, J. Y.; Wang, J. P.; Huang, W.; Yu, T. Strain-induced direct-indirect bandgap transition and phonon modulation in monolayer WS_2. *Nano Res.* **2015**, *8*, 2562−2572.
(36) Wu, J. B.; Wang, H.; Li, X. L.; Peng, H. L.; Tan, P. H. Raman spectroscopic characterization of stacking configuration and interlayer coupling of twisted multilayer graphene grown by chemical vapor deposition. *Carbon* **2016**, *110*, 225−231.

https://doi.org/10.1021/acs.chemmater.0c04799
Chem. Mater. 2021, 33, 2506−2515

(37) Zhang, X.; Tan, Q. H.; Wu, J. B.; Shi, W.; Tan, P. H. Review on the Raman spectroscopy of different types of layered materials. *Nanoscale* **2016**, *8*, 6435−6450.
(38) Beams, R.; Cancado, L. G.; Novotny, L. Raman characterization of defects and dopants in graphene. *J. Phys.: Condens. Matter* **2015**, *27*, No. 083002.
(39) Yoon, D.; Son, Y. W.; Cheong, H. Strain-Dependent Splitting of the Double-Resonance Raman Scattering Band in Graphene. *Phys. Rev. Lett.* **2011**, *106*, No. 155502.
(40) Lee, J. E.; Ahn, G.; Shim, J.; Lee, Y. S.; Ryu, S. Optical separation of mechanical strain from charge doping in graphene. *Nat. Commun.* **2012**, *3*, No. 1024.
(41) Mohiuddin, T. M. G.; Lombardo, A.; Nair, R. R.; Bonetti, A.; Savini, G.; Jalil, R.; Bonini, N.; Basko, D. M.; Galiotis, C.; Marzari, N.; Novoselov, K. S.; Geim, A. K.; Ferrari, A. C. Uniaxial strain in graphene by Raman spectroscopy: G peak splitting, Gruneisen parameters, and sample orientation. *Phys. Rev. B* **2009**, *79*, No. 205433.
(42) Xu, K.; Cao, P. G.; Heath, J. R. Scanning Tunneling Microscopy Characterization of the Electrical Properties of Wrinkles in Exfoliated Graphene Monolayers. *Nano Lett.* **2009**, *9*, 4446−4451.
(43) Piscanec, S.; Lazzeri, M.; Robertson, J.; Ferrari, A. C.; Mauri, F. Optical phonons in carbon nanotubes: Kohn anomalies, Peierls distortions, and dynamic effects. *Phys. Rev. B* **2007**, *75*, No. 035427.
(44) Ferrari, A. C. Raman spectroscopy of graphene and graphite: Disorder, electron-phonon coupling, doping and nonadiabatic effects. *Solid State Commun.* **2007**, *143*, 47−57.
(45) Ni, Z. H.; Wang, Y. Y.; Yu, T.; Shen, Z. X. Raman Spectroscopy and Imaging of Graphene. *Nano Res.* **2008**, *1*, 273−291.
(46) Zabel, J.; Nair, R. R.; Ott, A.; Georgiou, T.; Geim, A. K.; Novoselov, K. S.; Casiraghi, C. Raman Spectroscopy of Graphene and Bilayer under Biaxial Strain: Bubbles and Balloons. *Nano Lett.* **2012**, *12*, 617−621.
(47) Yi, D.; Yang, L.; Xie, S. J.; Saxena, A. Stability of hydrogenated graphene: a first-principles study. *RSC Adv.* **2015**, *5*, 20617−20622.
(48) Kresse, G.; Furthmuller, J. Efficiency of ab-initio total energy calculations for metals and semiconductors using a plane-wave basis set. *Comput. Mater. Sci.* **1996**, *6*, 15−50.
(49) Perdew, J. P.; Burke, K.; Ernzerhof, M. Generalized gradient approximation made simple. *Phys. Rev. Lett.* **1996**, *77*, No. 3865.
(50) Blöchl, P. E. Projector Augmented-Wave Method. *Phys. Rev. B* **1994**, *50*, No. 17953.
(51) Tkatchenko, A.; Scheffler, M. Accurate Molecular Van Der Waals Interactions from Ground-State Electron Density and Free-Atom Reference Data. *Phys. Rev. Lett.* **2009**, *102*, No. 073005.
(52) Brenner, D. W.; Shenderova, O. A.; Harrison, J. A.; Stuart, S. J.; Ni, B.; Sinnott, S. B. A second-generation reactive empirical bond order (REBO) potential energy expression for hydrocarbons. *J. Phys.: Condens. Matter* **2002**, *14*, 783−802.
(53) Berendsen, H. J. C.; Postma, J. P. M.; van Gunsteren, W. F.; DiNola, A.; Haak, J. R. Molecular dynamics with coupling to an external bath. *J. Chem. Phys.* **1984**, *81*, 3684−3690.
(54) Huang, Y.; Sutter, E.; Shi, N. N.; Zheng, J. B.; Yang, T. Z.; Englund, D.; Gao, H. J.; Sutter, P. Reliable Exfoliation of Large-Area High-Quality Flakes of Graphene and Other Two-Dimensional Materials. *ACS Nano* **2015**, *9*, 10612−10620.

https://doi.org/10.1021/acs.chemmater.0c04799
Chem. Mater. 2021, 33, 2506−2515